The Astrophysical Journal Letters, 953:L22 (13pp), 2023 August 20 https://doi.org/10.3847/2041-8213/acec6e

First Detection of X-Ray Polarization from the Accreting Neutron Star 4U 1820−303

Alessandro Di Marco[1], Fabio La Monaca[1], Juri Poutanen[2], Thomas D. Russell[3], Alessio Anitra[4], Ruben Farinelli[5], Guglielmo Mastroserio[6], Fabio Muleri[1], Fei Xie[1,7], Matteo Bachetti[6], Luciano Burderi[8], Francesco Carotenuto[9], Melania Del Santo[3], Tiziana Di Salvo[4], Michal Dovčiak[10], Andrea Gnarini[11], Rosario Iaria[4], Jari J. E. Kajava[2,12], Kuan Liu[7], Riccardo Middei[13,14], Stephen L. O'Dell[15], Maura Pilia[6], John Rankin[1], Andrea Sanna[8], Jakob van den Eijnden[16], Martin C. Weisskopf[15], Anna Bobrikova[2], Fiamma Capitanio[1], Enrico Costa[1], Philip Kaaret[15], Alessio Marino[17], Paolo Soffitta[1], Francesco Ursini[11], Filippo Ambrosino[13], Massimo Cocchi[6], Sergio Fabiani[1], Herman L. Marshall[18], Giorgio Matt[11], Sara Elisa Motta[19], Alessandro Papitto[13], Luigi Stella[13], Antonella Tarana[20], Silvia Zane[21], Iván Agudo[22], Lucio A. Antonelli[13,14], Luca Baldini[23,24], Wayne H. Baumgartner[15], Ronaldo Bellazzini[23], Stefano Bianchi[11], Stephen D. Bongiorno[15], Raffaella Bonino[25,26], Alessandro Brez[23], Niccolò Bucciantini[27,28,29], Simone Castellano[23], Elisabetta Cavazzuti[30], Chien-Ting Chen[31], Stefano Ciprini[14,32], Alessandra De Rosa[1], Ettore Del Monte[1], Laura Di Gesu[30], Niccolò Di Lalla[33], Immacolata Donnarumma[30], Victor Doroshenko[34], Steven R. Ehlert[15], Teruaki Enoto[35], Yuri Evangelista[1], Riccardo Ferrazzoli[1], Javier A. Garcia[36], Shuichi Gunji[37], Kiyoshi Hayashida[38,62], Jeremy Heyl[39], Wataru Iwakiri[40], Svetlana G. Jorstad[41,42], Vladimir Karas[10], Fabian Kislat[43], Takao Kitaguchi[35], Jeffery J. Kolodziejczak[15], Henric Krawczynski[44], Luca Latronico[25], Ioannis Liodakis[45], Simone Maldera[25], Alberto Manfreda[46], Frédéric Marin[47], Andrea Marinucci[30], Alan P. Marscher[41], Francesco Massaro[25,26], Ikuyuki Mitsuishi[48], Tsunefumi Mizuno[49], Michela Negro[50,51,52], Chi-Yung Ng[53], Nicola Omodei[33], Chiara Oppedisano[25], George G. Pavlov[54], Abel L. Peirson[33], Matteo Perri[13,14], Melissa Pesce-Rollins[23], Pierre-Olivier Petrucci[55], Andrea Possenti[6], Simonetta Puccetti[14], Brian D. Ramsey[15], Ajay Ratheesh[1], Oliver J. Roberts[31], Roger W. Romani[33], Carmelo Sgrò[23], Patrick Slane[56], Gloria Spandre[23], Douglas A. Swartz[31], Toru Tamagawa[35], Fabrizio Tavecchio[57], Roberto Taverna[58], Yuzuru Tawara[48], Allyn F. Tennant[15], Nicholas E. Thomas[15], Francesco Tombesi[32,59,60], Alessio Trois[6], Sergey S. Tsygankov[2], Roberto Turolla[21,58], Jacco Vink[61], and Kinwah Wu[21]
(IXPE Collaboration)

[1] INAF Istituto di Astrofisica e Planetologia Spaziali, Via del Fosso del Cavaliere 100, I-00133 Roma, Italy; alessandro.dimarco@inaf.it
[2] Department of Physics and Astronomy, FI-20014 University of Turku, Finland
[3] INAF, Istituto di Astrofisica Spaziale e Fisica Cosmica, Via U. La Malfa 153, I-90146 Palermo, Italy
[4] Università degli Studi di Palermo, Dipartimento di Fisica e Chimica, Emilio Segrè, via Archirafi 36 I-90123 Palermo, Italy
[5] INAF, Osservatorio di Astrofisica e Scienza dello Spazio di Bologna, Via P. Gobetti 101, I-40129 Bologna, Italy
[6] INAF, Osservatorio Astronomico di Cagliari, Via della Scienza 5, I-09047 Selargius (CA), Italy
[7] Guangxi Key Laboratory for Relativistic Astrophysics, School of Physical Science and Technology, Guangxi University, Nanning 530004, People's Republic of China
[8] Dipartimento di Fisica, Università degli Studi di Cagliari, SP Monserrato-Sestu km 0.7, I-09042 Monserrato, Italy
[9] Department of Physics, Astrophysics, University of Oxford, Denys Wilkinson Building, Keble Road, Oxford OX1 3RH, UK
[10] Astronomical Institute of the Czech Academy of Sciences, Boční II 1401/1, 14100 Praha 4, Czech Republic
[11] Dipartimento di Matematica e Fisica, Università degli Studi Roma Tre, Via della Vasca Navale 84, I-00146 Roma, Italy
[12] Serco for the European Space Agency (ESA), European Space Astronomy Centre (ESAC), Camino Bajo del Castillo s/n, E-28692 Villanueva de la Cañada, Madrid, Spain
[13] INAF, Osservatorio Astronomico di Roma, Via Frascati 33, I-00040 Monte Porzio Catone (RM), Italy
[14] Space Science Data Center, Agenzia Spaziale Italiana, Via del Politecnico snc, I-00133 Roma, Italy
[15] NASA Marshall Space Flight Center, Huntsville, AL 35812, USA
[16] Department of Physics, University of Warwick, Coventry, CV4 7AL, UK
[17] Institute of Space Sciences (ICE-CSIC), Barcelona, Spain
[18] MIT Kavli Institute for Astrophysics and Space Research, Massachusetts Institute of Technology, 77 Massachusetts Avenue, Cambridge, MA 02139, USA
[19] INAF, Osservatorio Astronomico di Brera, Via E. Bianchi 46, I-23807 Merate (LC), Italy
[20] Liceo Scientifico F. Enriques, via F. Paolini, 196, I-00122, Ostia (Rome), Italy
[21] Mullard Space Science Laboratory, University College London, Holmbury St Mary, Dorking, Surrey RH5 6NT, UK
[22] Instituto de Astrofísicade Andalucía—CSIC, Glorieta de la Astronomía s/n, E-18008 Granada, Spain
[23] Istituto Nazionale di Fisica Nucleare, Sezione di Pisa, Largo B. Pontecorvo 3, I-56127 Pisa, Italy
[24] Dipartimento di Fisica, Università di Pisa, Largo B. Pontecorvo 3, I-56127 Pisa, Italy
[25] Istituto Nazionale di Fisica Nucleare, Sezione di Torino, Via Pietro Giuria 1, I-10125 Torino, Italy
[26] Dipartimento di Fisica, Università degli Studi di Torino, Via Pietro Giuria 1, I-10125 Torino, Italy
[27] INAF, Osservatorio Astrofisico di Arcetri, Largo Enrico Fermi 5, I-50125 Firenze, Italy
[28] Dipartimento di Fisica e Astronomia, Università degli Studi di Firenze, Via Sansone 1, I-50019 Sesto Fiorentino (FI), Italy
[29] Istituto Nazionale di Fisica Nucleare, Sezione di Firenze, Via Sansone 1, I-50019 Sesto Fiorentino (FI), Italy
[30] Agenzia Spaziale Italiana, Via del Politecnico snc, I-00133 Roma, Italy
[31] Science and Technology Institute, Universities Space Research Association, Huntsville, AL 35805, USA
[32] Istituto Nazionale di Fisica Nucleare, Sezione di Roma "Tor Vergata," Via della Ricerca Scientifica 1, I-00133 Roma, Italy
[33] Department of Physics and Kavli Institute for Particle Astrophysics and Cosmology, Stanford University, Stanford, CA 94305, USA
[34] Institut für Astronomie und Astrophysik, Universität Tübingen, Sand 1, D-72076 Tübingen, Germany
[35] RIKEN Cluster for Pioneering Research, 2-1 Hirosawa, Wako, Saitama 351-0198, Japan
[36] California Institute of Technology, Pasadena, CA 91125, USA
[37] Yamagata University, 1-4-12 Kojirakawa-machi, Yamagata-shi 990-8560, Japan
[38] Osaka University, 1-1 Yamadaoka, Suita, Osaka 565-0871, Japan

[39] University of British Columbia, Vancouver, BC V6T 1Z4, Canada
[40] International Center for Hadron Astrophysics, Chiba University, Chiba 263-8522, Japan
[41] Institute for Astrophysical Research, Boston University, 725 Commonwealth Avenue, Boston, MA 02215, USA
[42] Department of Astrophysics, St. Petersburg State University, Universitetsky pr. 28, Petrodvoretz, 198504 St. Petersburg, Russia
[43] Department of Physics and Astronomy and Space Science Center, University of New Hampshire, Durham, NH 03824, USA
[44] Physics Department and McDonnell Center for the Space Sciences, Washington University in St. Louis, St. Louis, MO 63130, USA
[45] Finnish Centre for Astronomy with ESO, FI-20014 University of Turku, Finland
[46] Istituto Nazionale di Fisica Nucleare, Sezione di Napoli, Strada Comunale Cinthia, I-80126 Napoli, Italy
[47] Université de Strasbourg, CNRS, Observatoire Astronomique de Strasbourg, UMR 7550, F-67000 Strasbourg, France
[48] Graduate School of Science, Division of Particle and Astrophysical Science, Nagoya University, Furo-cho, Chikusa-ku, Nagoya, Aichi 464-8602, Japan
[49] Hiroshima Astrophysical Science Center, Hiroshima University, 1-3-1 Kagamiyama, Higashi-Hiroshima, Hiroshima 739-8526, Japan
[50] University of Maryland, Baltimore County, Baltimore, MD 21250, USA
[51] NASA Goddard Space Flight Center, Greenbelt, MD 20771, USA
[52] Center for Research and Exploration in Space Science and Technology, NASA/GSFC, Greenbelt, MD 20771, USA
[53] Department of Physics, University of Hong Kong, Pokfulam, Hong Kong
[54] Department of Astronomy and Astrophysics, Pennsylvania State University, University Park, PA 16801, USA
[55] Université Grenoble Alpes, CNRS, IPAG, F-38000 Grenoble, France
[56] Center for Astrophysics, Harvard & Smithsonian, 60 Garden St, Cambridge, MA 02138, USA
[57] INAF, Osservatorio Astronomico di Brera, via E. Bianchi 46, I-23807 Merate (LC), Italy
[58] Dipartimento di Fisica e Astronomia, Università degli Studi di Padova, Via Marzolo 8, I-35131 Padova, Italy
[59] Dipartimento di Fisica, Università degli Studi di Roma "Tor Vergata," Via della Ricerca Scientifica 1, I-00133 Roma, Italy
[60] Department of Astronomy, University of Maryland, College Park, MD 20742, USA
[61] Anton Pannekoek Institute for Astronomy & GRAPPA, University of Amsterdam, Science Park 904, 1098 XH Amsterdam, The Netherlands
Received 2023 June 14; revised 2023 July 31; accepted 2023 July 31; published 2023 August 18

Abstract

This paper reports the first detection of polarization in the X-rays for atoll-source 4U 1820−303, obtained with the Imaging X-ray Polarimetry Explorer (IXPE) at 99.999% confidence level (CL). Simultaneous polarimetric measurements were also performed in the radio with the Australia Telescope Compact Array. The IXPE observations of 4U 1820−303 were coordinated with Swift X-ray Telescope, Neutron Star Interior Composition Explorer, and Nuclear Spectroscopic Telescope Array aiming to obtain an accurate X-ray spectral model covering a broad energy interval. The source shows a significant polarization above 4 keV, with a polarization degree of $2.0\% \pm 0.5\%$ and a polarization angle of $-55^\circ \pm 7^\circ$ in the 4–7 keV energy range, and a polarization degree of $10\% \pm 2\%$ and a polarization angle of $-67^\circ \pm 7^\circ$ in the 7–8 keV energy bin. This polarization also shows a clear energy trend with polarization degree increasing with energy and a hint for a position-angle change of $\simeq 90^\circ$ at 96% CL around 4 keV. The spectro-polarimetric fit indicates that the accretion disk is polarized orthogonally to the hard spectral component, which is presumably produced in the boundary/spreading layer. We do not detect linear polarization from the radio counterpart, with a 3σ upper limit of 50% at 7.25 GHz.

Unified Astronomy Thesaurus concepts: Low-mass x-ray binary stars (939); Neutron stars (1108); Polarimetry (1278); Spectropolarimetry (1973); Stellar accretion disks (1579)

1. Introduction

Accreting weakly magnetized neutron stars (NSs) in low-mass X-ray binaries (LMXBs) are among the brightest X-ray sources; they accrete matter via Roche lobe overflow from a stellar companion of mass typically lower than a solar mass (Bahramian & Degenaar 2022). They can be classified according to the shape of their tracks in the X-ray hard-color/soft-color diagram (CCD), or their hard-color/intensity diagram (HID), and their correlated timing in the 1–10 keV band (Hasinger & van der Klis 1989; van der Klis 1989). The following states are known: (i) the high soft state (HSS) of Z-sources with a luminosity $>10^{37}$ erg s^{-1} (near-Eddington X-ray luminosities) exhibiting a wide Z-like shape in the CCD; (ii) the low hard state (LHS) of atoll sources with a luminosity $\simeq 10^{36}$ erg s^{-1} showing a single rounded spot in the CCD (island state) typically and having a harder spectrum than HSS; (iii) the HSS of bright atoll sources, having intermediate luminosities (10^{36}–10^{37} erg s^{-1}), typically following a banana shape figure in the CCD. The banana state has been further divided on the basis of their luminosity into left-lower (lower luminosity), upper (higher luminosity), and lower banana in the middle.

The spectral and timing properties of these sources provide clues to their emission mechanisms, and their X-ray emission generally is described by two main spectral components: (i) a soft thermal component (blackbody-like emission from the NS surface or from the accretion disk); (ii) a harder component associated with the interaction of the accretion disk with the NS surface. The interaction region that is coplanar to the accretion disk is called the boundary layer (BL; Shakura & Sunyaev 1988; Popham & Sunyaev 2001), while the gas layer at the NS surface, extending up to high latitudes, is called the spreading layer (SL; Inogamov & Sunyaev 1999; Suleimanov & Poutanen 2006). The properties of the SL/BL region (temperature and optical depth) clearly distinguish sources in the LHS from the ones in the HSS, with the former SL/BL much hotter and more transparent with respect to the latter ones (Gnarini et al. 2022). The frequent observation of a reflection component, whose most prominent feature is an iron emission line at ~ 6.5 keV, suggests Compton reflection by a colder medium (e.g., the outer accretion disk itself) as a further

[62] Deceased.

component to take into account, especially in the HSS (see, e.g., Cackett et al. 2008; Egron et al. 2013; Titarchuk et al. 2013; Mondal et al. 2016).

The launch of the Imaging X-ray Polarimetry Explorer (IXPE), in 2021 December (Soffitta et al. 2021; Weisskopf et al. 2022), gave us the opportunity to use X-ray polarization, in addition to spectral and timing information, to disentangle several scenarios. The X-ray polarization of weakly magnetized NSs strongly depends on the geometry of the emission region. In the LHS sources, it can be produced by a non-spherical slab-like corona (as in the case of BH-LMXB, Haardt & Matt 1993; Poutanen & Vilhu 1993; Poutanen & Svensson 1996; Schnittman & Krolik 2010), or by the accretion disk (Chandrasekhar 1960; Loskutov & Sobolev 1982). In the HSS sources, the BL and the SL (Lapidus & Sunyaev 1985) emission can be polarized; also, Comptonization of any seed soft photons in a corona and reflection of the SL radiation off the accretion disk are potential sources of polarized emission (Lapidus & Sunyaev 1985; Suleimanov & Poutanen 2006; D'Aì 2010).

In order to investigate the geometry of the accretion flow in LMXBs, IXPE has so far targeted several sources: the Z-source Cyg X-2 (Farinelli et al. 2023), the Z-atoll transient source XTE J1701−462 (Cocchi et al. 2023; Jayasurya et al. 2023), and two atoll sources, GS 1826−238 (Capitanio et al. 2023) and GX 9+9 (Chatterjee et al. 2023; Ursini et al. 2023). These observations found a higher polarization in the Z-sources than in the atoll ones; moreover, the polarization angle (PA) of Cyg X-2, for the hardest part of the energy spectrum, appears to be aligned with the radio jet. Also, a marginal detection of polarization available for Sco X-1 from OSO-8 (Long et al. 1979) and PolarLight (Long et al. 2022) appears to show such an alignment between the radio jet and the PA. An attempt to measure the X-ray polarization of 4U 1820−303 was performed by OSO-8 (Hughes et al. 1984), but only 99% confidence level (CL) upper limits of 4.7% and 10.8% were obtained at 2.6 and 5.2 keV, respectively.

4U 1820−303 is an ultra-compact LMXB consisting of an NS, accreting matter via Roche lobe overflow from a He white dwarf. It is located at $0\farcs66$ from the center of the globular cluster NGC 6624 (Rappaport et al. 1987; Shaposhnikov & Titarchuk 2004), and its distance was estimated from the GAIA EDR3 to be $D = 8.0 \pm 0.1$ kpc (Baumgardt & Vasiliev 2021). 4U 1820−303 has an orbital period of 685 s (Stella et al. 1987) and a peculiar behavior with intrinsic luminosity variation by a factor of at least 2 along a superorbital ∼170 days period (Zdziarski et al. 2007). Chou & Grindlay (2001) found the flux modulation to be stable in the period 1969–2000 with periodicity 171.0 ± 0.3 days, compatible with the RXTE All Sky Monitor data (Zdziarski et al. 2007). These variations are also seen in the Monitor of All-sky X-ray Image (MAXI) and the Swift Burst Alert Telescope (Swift-BAT) light curves (see Figure 1). 4U 1820−303 is the first identified source of type-I X-ray bursts (Grindlay et al. 1976), observed mainly around the flux minima, proving that the observed variability is indeed due to intrinsic accretion rate changes; this is also supported by the strong correlations between the observed flux variations with the source spectral state (in a way typical of atoll-type NS binaries) and the kHz frequency of quasi-periodic oscillations (Smale et al. 1997).

4U 1820−303, as typically observed in weakly magnetized NS-LMXBs, shows a spectrum mainly composed of two components:

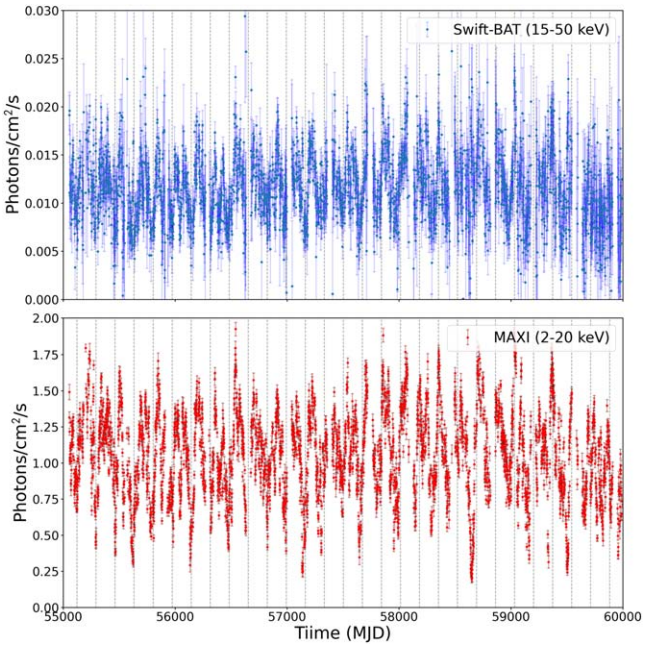

Figure 1. Light curves from Swift-BAT monitor in the 15–50 keV energy band (top) and MAXI in 2–20 keV energy band (bottom). The dashed vertical lines identify the 170 days superorbital period.

a blackbody or multicolor disk that describes the softer spectral component, and a Comptonization to describe the harder spectral one. Moreover, these sources can show a component due to reflection, which has, as a main feature, the presence of a Gaussian due to the iron Kα lines at ∼6.5 keV (Cackett et al. 2008; Titarchuk et al. 2013; Mondal et al. 2016). 4U 1820−303 shows a broad iron line (Mondal et al. 2016), which Cackett et al. (2008) fitted with a `diskline` obtaining the disk inclination of ∼20°.

4U 1820−303 is also a known radio emitter (e.g., Migliari et al. 2004; Díaz Trigo et al. 2017; Russell et al. 2021). At low X-ray fluxes, the radio spectrum is typically observed to be relatively flat, consistent with a compact radio jet, while, at higher X-ray fluxes (Russell et al. 2021), the radio spectrum becomes steep, consistent with either a quenching of the compact jet emission or emission from a transient jet ejecta (Russell et al. 2021). Assuming a uniform and ordered magnetic field, linear polarization from a compact (self-absorbed) radio jet is expected to have a maximum degree of ∼10%, while the optically thin ejecta can exhibit values up to ∼70% (see pp. 217–222 in Longair 2011); however, due to disorder in the magnetic fields, lower values are typically observed (see, e.g., Curran et al. 2014).

2. X-Ray Observations

IXPE observed 4U 1820−303 in two different periods: on 2022 October 11 from 13:53 to 22:55 UTC for a total exposure of ≃16 ks per detector unit (DU) and from 2023 April 15 01:33 to April 16 23:17 UTC for a total exposure of ≃86 ks per DU. During these periods, other observatories performed simultaneous observations. To determine the state of 4U 1820−303 during the IXPE observations, we analyzed the daily count rates in the 2–20 keV energy band from MAXI telescope[63]

[63] http://maxi.riken.jp/top/index.html

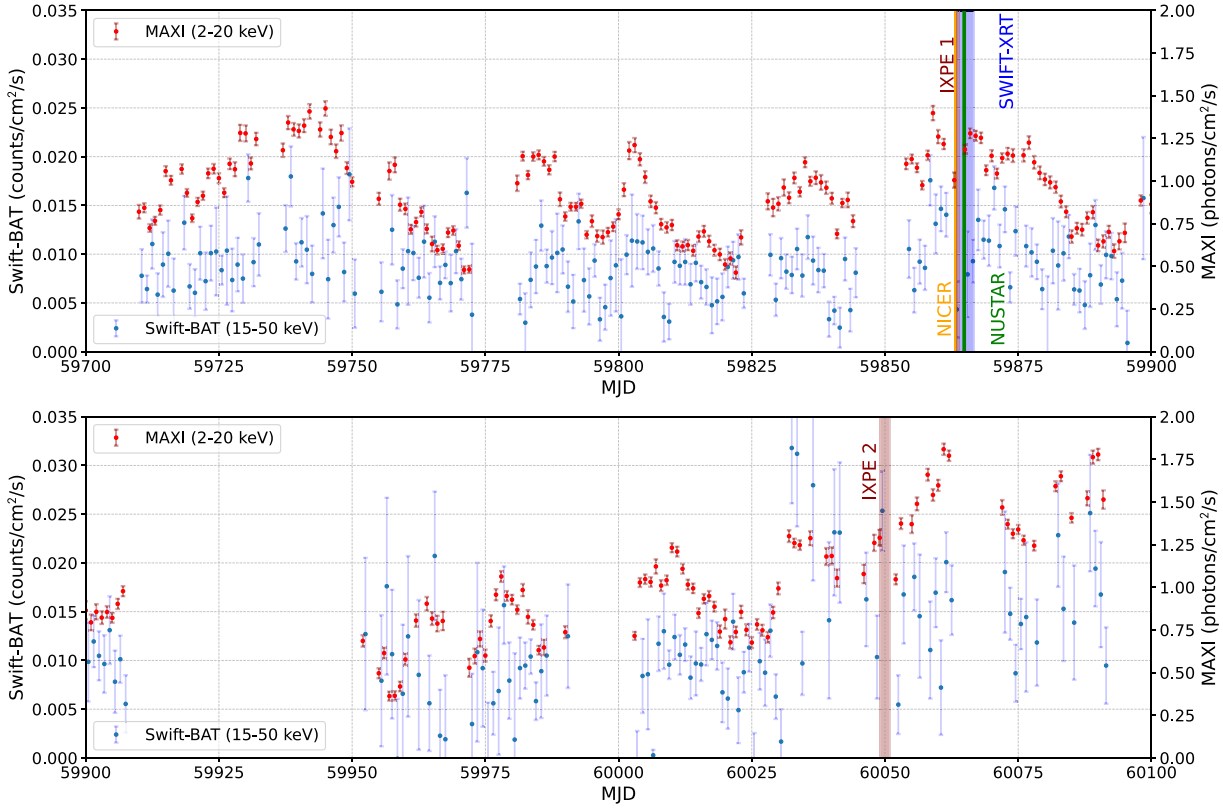

Figure 2. Light curves from Swift-BAT in the 15–50 keV energy band (blue points) and MAXI in the 2–20 keV energy band (red points); overlaid in dark red are the IXPE intervals of observation. For the first observation (top panel), where coordinated observations were not strictly simultaneous, vertical bands show the observing period for NICER (orange), NuSTAR (green), and Swift-XRT (blue), while for the second (bottom panel) they were strictly simultaneous and included in the IXPE band.

(Matsuoka et al. 2009), and in the 15–50 keV band from the Swift-BAT Hard X-ray Transient Monitor[64] (Krimm et al. 2013). The 4U 1820−303 light curves, covering since 2009 August from both observatories, are shown in Figure 1. IXPE observations were performed near the maximum of the flux along the superorbital period, as shown in Figure 2.

In Figure 3, we show the corresponding HID, where the hardness is given by the ratio between Swift-BAT count rate in the 15–50 keV band and the MAXI count rate in the 2–4 keV band, and the flux is represented by the MAXI count rate in the 2–20 keV band. The red points report the state of the source along our coordinated observations: (1) on 2022 October 11, by Neutron Star Interior Composition Explorer (NICER), IXPE, and Swift X-ray Telescope (XRT); (2) on 2022 October 12, by Swift-XRT and the Nuclear Spectroscopic Telescope Array (NuSTAR); (3) on 2022 October 13, by Swift-XRT; (4) on 2023 April 15, by IXPE, Swift-XRT, NICER, and NuSTAR and Australia Telescope Compact Array (ATCA); (5) on 2023 April 16, by IXPE, NICER, NuSTAR, and Swift-XRT. From this HID, we observe that the source was in the lower banana state in all of them. To further confirm this result, we used coordinated Swift-XRT data to monitor the hardness ratio (HR) along the two periods of observations; we defined the Swift-XRT HR as follows:

$$\mathrm{HR} = \frac{\text{counts in 4–10 keV} - \text{counts in 0.3–4 keV}}{\text{counts in 0.3–10 keV}}. \quad (1)$$

[64] https://swift.gsfc.nasa.gov/results/transients/

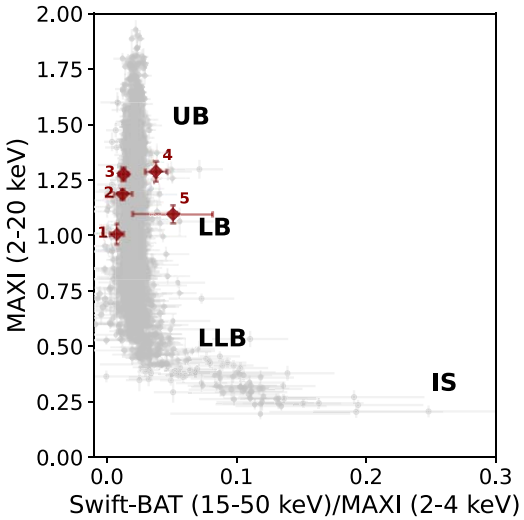

Figure 3. Hardness–intensity diagram, where the different states of the source are identified: the island state (IS), where the source has a harder spectrum; the softer banana state with upper banana (UB), lower banana (LB), and left lower banana (LLB). The red points report the source state during the first and the second IXPE coordinated observations at the times discussed in the text.

Figure 4 shows this HR as a function of time near the first IXPE pointing—when, because of the brightest ever gamma-ray burst (Burns et al. 2023), the IXPE observations were stopped, and other observatories were not able to perform strictly simultaneous observations—and near the second IXPE pointing when all the observations with other telescopes were strictly simultaneous.

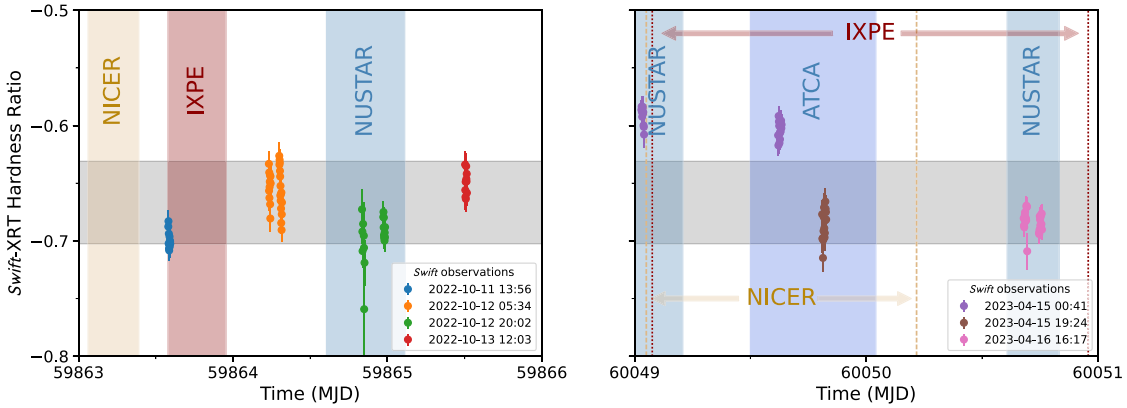

Figure 4. Swift-XRT HR in time bins of 100 s during the first (left, we used ObsIDs: 00014980028, 00014980029, 00014980030, and 00014980031) and the second (right, we used ObsIDs: 00014980055, 00014980056, and 00014980057) IXPE coordinated observations. The horizontal gray band reports the average 99% CL HR interval during the two observations; the vertical bands and/or horizontal arrows report the time intervals when observations by other observatories were performed.

From this analysis, we can confirm that the HR values fluctuate around an average HR band as shown in Figure 4, thus, the source has not changed its state; only the data from observation ID (ObsID) 00014980055 (on April 15 since 00:41) show a slightly harder spectrum, but this hardening corresponds to a slightly higher counting rate, and it can be explained as due to pile-up (Romano et al. 2006). Also from the NuSTAR HR, assuming the soft component in 3–10 keV and the harder one in 10–30 keV, we see that HR does not vary much. Thus, for the following spectral and spectro-polarimetric analysis, we join the data from the different observations to improve the sensitivity.

3. Polarimetric Analysis

IXPE observed 4U 1820−303 twice, both times during its lower banana state; this suggests that the two observations have the same spectral properties, allowing us to merge them. From the point of view of the polarization, due to the lack of significant measurements before IXPE, this is something that we need to confirm by comparing the polarization in the first and in the second observation. At this aim, we used the IXPEOBSSIM software (Baldini et al. 2022) with the `PCUBE` algorithm to have a preliminary estimate of polarization. In the IXPE data, the background is negligible (roughly 2 orders of magnitude below the source in the whole energy band); thus, the prescription reported in Di Marco et al. (2023) for bright sources have been applied.

IXPE in its nominal energy band reports an average polarization that is not significant in the first observation and has a low significance in the second. Also combining the two data sets, we obtain a polarization below the 99% CL. The polarimetric analysis was performed using two energy bins: 2–4 and 4–8 keV, as reported in Figures 5(a) and (b). The contour regions resulting from the two IXPE observations in both the energy bins are compatible allowing to combine the two data sets.

We performed a study of the polarization using the combined data from the two IXPE observations by using the `PCUBE` analysis to measure the normalized Stokes parameters as a function of the energy with bins of 1 keV; the results are shown in Figure 6, and reported in Table 1. We obtain that only the energy bin 7–8 keV has a highly significant polarization at 99.99% CL. On the other hand, taking into account each energy bin as an independent data set, the statistical significance of this observation in any one bin has been evaluated; then, the CL for the polarization detection was tested assuming the ensemble of bins against the null hypothesis (i.e., assuming a null polarization in every bin). The result of this test allowed us to obtain a probability of null polarization of 5.32×10^{-6}, which correspond to a polarization detection at level of 99.995% CL. Moreover, we see that the Stokes parameters show a clear trend of the polarization degree (PD) increasing with energy. We identify three energy ranges showing similar polarization from Figure 6: 2–4, 4–7, and 7–8 keV. By grouping the data within these wider bins, we can increase the significance of detection both in each bin (2–4 and 4–7 keV have a polarization detection at 96% and 99.97% CL, respectively) and for the whole set of bins reaching a 99.99997% CL. The resulting PD and PA contour plots for the three wider bins are shown in Figure 5(c), while the numerical results are reported in Table 1. The most significant polarization is measured at CL $>99.99\%$ in the 7–8 keV energy bin, where the PD reaches a value of $\sim$10%, never observed in other weakly magnetized sources (Capitanio et al. 2023; Chatterjee et al. 2023; Cocchi et al. 2023; Farinelli et al. 2023; Jayasurya et al. 2023; Ursini et al. 2023). We also observe a position-angle change by nearly 90° between 2 and 4 keV, and the higher energy bins (significant at 96% CL).

4. Spectral Analysis

Using the data from NICER (in 0.7–12 keV) and NuSTAR (in 3–30 keV)—see Appendix for details about data extraction—and IXPE (in 2–8 keV) weighted spectra (Di Marco et al. 2022a) and on the basis of the spectral models present in the literature (Tarana et al. 2007; Titarchuk et al. 2013), we applied the model `tbabs*(diskbb+comptb)` in XSPEC v.12.13.0c (Arnaud 1996). To estimate the absorption from the interstellar medium, we set the abundances at the `wilm` values (Wilms et al. 2000). The NuSTAR residuals show an excess, as reported in Figure 7, compatible with the presence of a broad iron line, such an excess is not appreciable in the IXPE and NICER data.

Because of the excess in the NuSTAR residuals, we included in the model a Gaussian line: `tbabs*(diskbb+comptb +Gauss)`. The χ^2/degrees of freedom (dof) is 1955/1785 without a line, to compare with 1835/1780 when a line is included. Summarizing, the adopted best-fit model includes

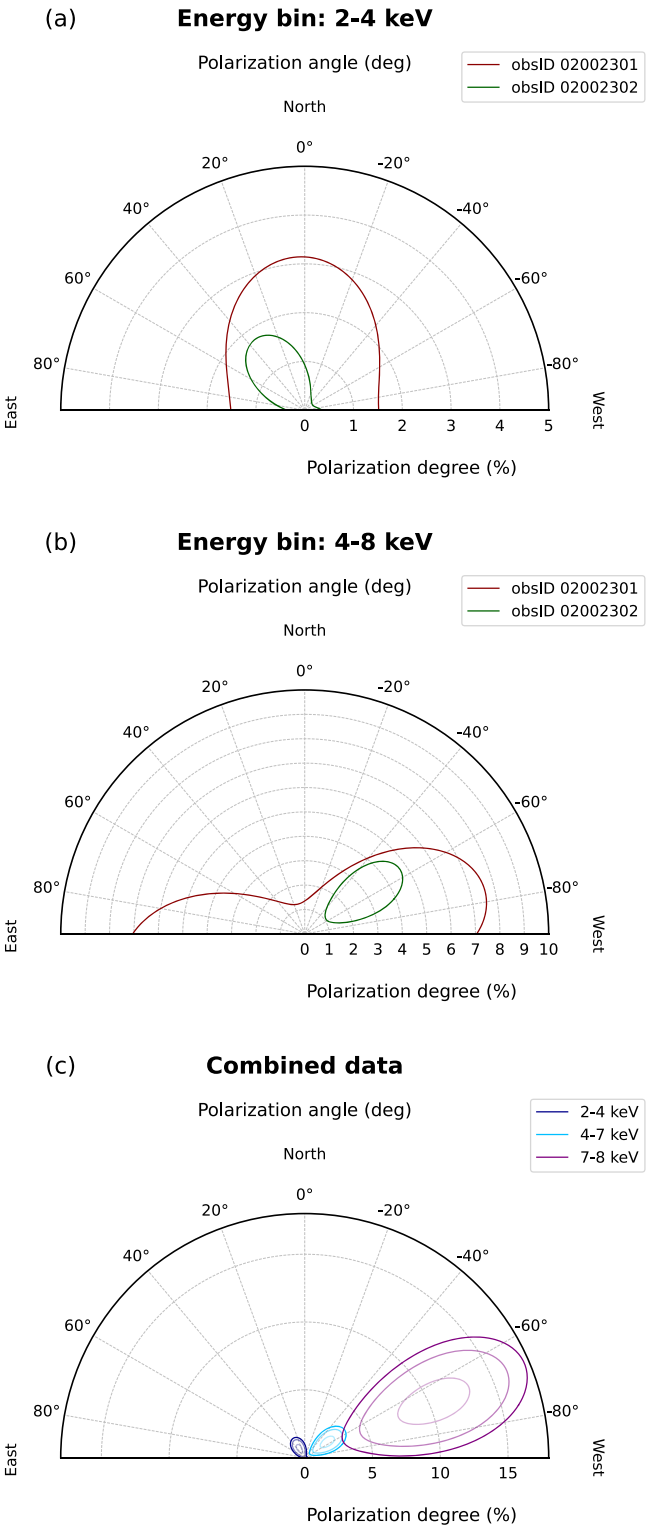

Figure 5. Polar plot of the X-ray polarization in 4U 1820−303. (a) Contours at 99% CL in the 2–4 keV energy bin, for the first (red) and the second (green) observations. (b) Same as (a), but in the 4–8 keV energy bin. (c) Combined data in the three energy bins 2–4, 4–7, and 7–8 keV. The contours correspond to 50%, 95%, and 99% CL.

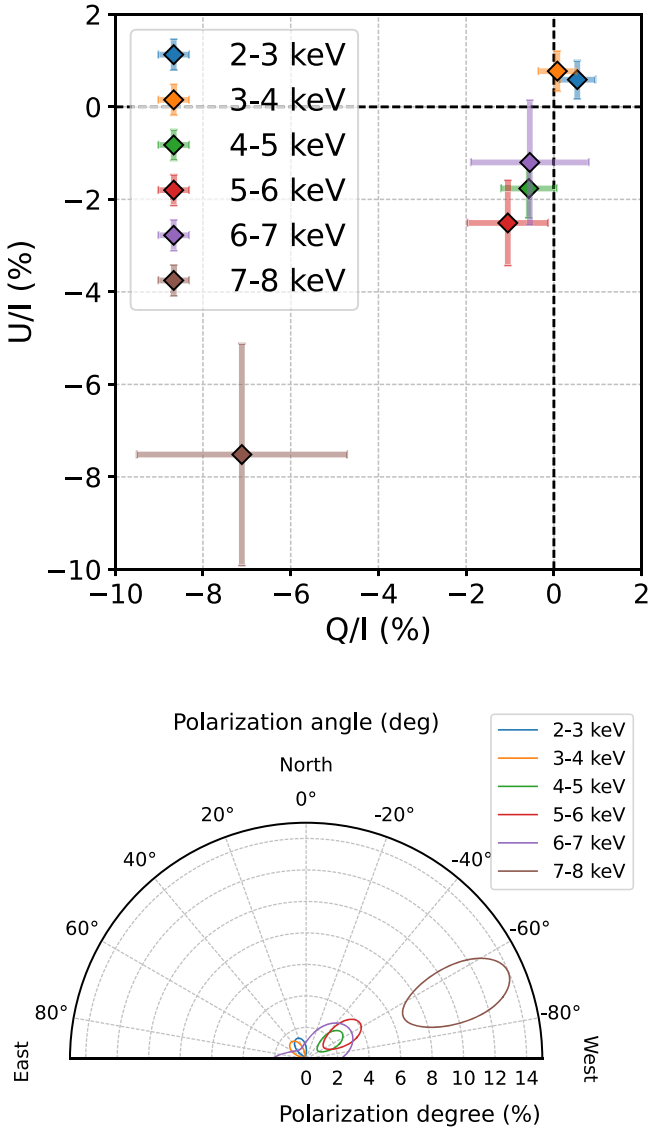

Figure 6. Top: normalized Stokes parameters Q/I and U/I in different energy bins as measured with PCUBE in IXPEOBSSIM. Bottom: polar plot of the X-ray polarization in 4U 1820−303 when 1 keV binning is applied. Contours are reported at 68% CL. A trend of polarization growing with energy is visible in both plots.

Table 1
Polarization Properties Obtained with the PCUBE Algorithm for the Merged Data from Both the IXPE Observations

Energy Bin (keV)	PD (%)	PA (deg)	Q/I (%)	U/I (%)
2–3	0.8 ± 0.4	24 ± 15	0.5 ± 0.4	0.6 ± 0.4
3–4	0.8 ± 0.4	42 ± 16	0.1 ± 0.4	0.8 ± 0.4
4–5	1.9 ± 0.6	-54 ± 10	-0.6 ± 0.6	-1.8 ± 0.6
5–6	2.7 ± 0.9	-56 ± 10	-1.1 ± 0.9	-2.5 ± 0.9
6–7	1.3 ± 1.3	-57 ± 29	-0.6 ± 1.3	-1.2 ± 1.3
7–8	10.3 ± 2.4	-67 ± 7	-7.1 ± 2.4	-7.5 ± 2.4
2–4	0.75 ± 0.30	30 ± 11	0.37 ± 0.30	0.66 ± 0.30
4–7	2.0 ± 0.5	-55 ± 7	-0.7 ± 0.5	-1.9 ± 0.5

Note. Errors are reported at 68% CL.

diskbb for the disk emission, Gauss for the Fe Kα line, and comptb (with bulk parameter $\delta = 0$) for thermal Comptonization with the seed photons following a blackbody distribution ($\Gamma = 3$) and a large Comptonized fraction $A \gg 1$ that is obtained by freezing $\log A = 5$. We tested also bbody for the soft component and the compTT for the harder one, obtaining similar results, but we opted for this spectral model that provides a better reduced χ^2.

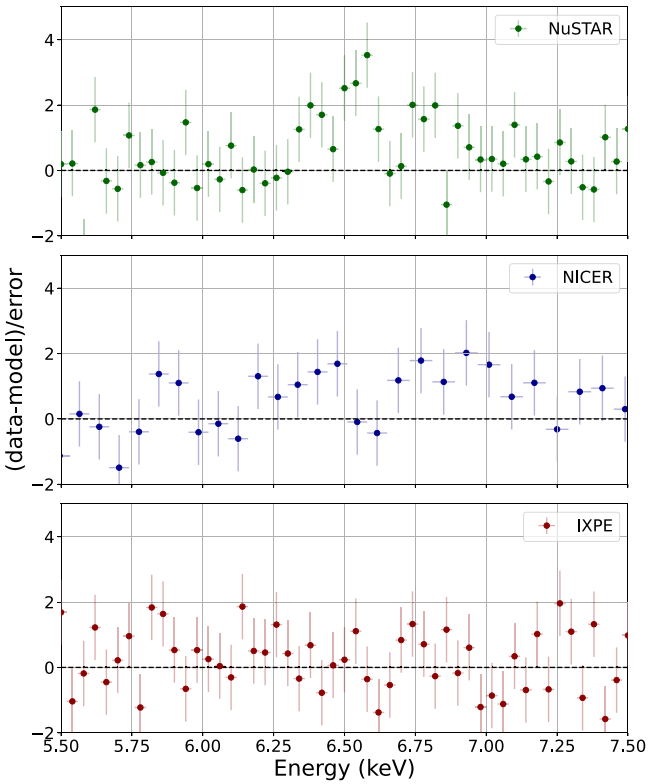

Figure 7. Energy spectra residuals in the energy range 5.5–7.5 keV from the 4U 1820−303 observations with NuSTAR (top), NICER (center), and IXPE (bottom), when the spectral model does not include the iron line. We see that NuSTAR data show an excess compatible with a broad iron line, not appreciable in IXPE and NICER data.

This model has been applied to fit a broadband spectrum of the combined simultaneous data set by NICER, NuSTAR, and IXPE. We also used the energy-independent cross-normalization factors. The best-fit parameters are summarized in Table 2. The EF_E spectrum and its residuals are reported in Figure 8.

To take into account NuSTAR calibration uncertainties (Madsen et al. 2022), we assumed a gain offset free in the fit, obtaining $-(0.085 \pm 0.009)$ keV and $-(0.068 \pm 0.008)$ keV for the focal plane modules A and B (FPMA and FPMB), respectively; similarly for IXPE calibration uncertainties (Di Marco et al. 2022b), we left free the gain slope and offset obtaining a slope of 0.981 ± 0.003, 0.973 ± 0.003, $0.980 \pm 0.003\,\mathrm{keV}^{-1}$ for the DU1, DU2, and DU3 respectively, while the offset in each one is 0.003 ± 0.012, 0.032 ± 0.012, and 0.020 ± 0.012 keV. As reported also by the photons fluxes of Table 2, the spectrum in the whole 2–8 keV IXPE energy band is dominated by the Comptonization component, while the disk contributes only at lower energies (see also Figure 8).

It is worth noting that the Fe line is typically found along with a broadband reflection component (e.g., Iaria et al. 2016; Ursini et al. 2023). We therefore tested several self-consistent models (such as `relxillns`) or convolution ones (such as `rdblur*rfxconv`) to take into account the reflection component. However, none of them produced a statistically significant improvement to the fit, and the reflection fraction was negligible (<5%). Since a more detailed treatment of the reflection goes beyond the scope of this manuscript, we did not include any reflection component in the following spectro-polarimetric modeling.

Table 2
Best-fit Parameters of the Spectral Model `tbabs(diskbb + comptb + Gauss)` Applied to the Simultaneous Data from NICER, NuSTAR, and IXPE

Model	Parameter	Value
`tbabs`	$N_{\rm H}$ ($\times 10^{22}$ cm^{-2})	0.14 ± 0.01
`diskbb`	$kT_{\rm in}$ (keV)	$0.52^{+0.03}_{-0.04}$
	norm ($[R_{\rm in}/D_{10}]^2 \cos\theta$)	1900^{+500}_{-400}
	$R_{\rm in}$ [a] (km)	40 ± 20
`comptb`	$kT_{\rm s}$ (keV)	0.72 ± 0.05
	α	0.93 ± 0.01
	$kT_{\rm e}$ (keV)	$2.919^{+0.016}_{-0.008}$
	$L_{\rm X}$ [b] ($\times 10^{39}$ erg s^{-1})	0.0347 ± 0.0004
`Gauss`	$E_{\rm line}$ (keV)	6.63 ± 0.09
	σ (keV)	0.56 ± 0.01
	norm (photon centimeters^{-2} second^{-1})	$0.0020^{+0.0006}_{-0.0005}$
	equivalent width (eV)	34.2 ± 1.2
	$\chi^2/\mathrm{dof} = 1835/1780 = 1.03$	
	Cross-normalization factors	
	$C_{\rm NICER}$	1.0
	$C_{\rm NuSTAR-A}$	1.063 ± 0.004
	$C_{\rm NuSTAR-B}$	1.057 ± 0.004
	$C_{\rm IXPE-DU1}$	1.034 ± 0.007
	$C_{\rm IXPE-DU2}$	0.990 ± 0.007
	$C_{\rm IXPE-DU3}$	0.932 ± 0.007
	Photon flux ratios in 2–8 keV	
	$F_{\rm diskbb}/F_{\rm tot}$	0.114
	$F_{\rm comptb}/F_{\rm tot}$	0.884
	$F_{\rm gauss}/F_{\rm tot}$	0.002

Notes. The estimated flux in 2–8 keV is 5.23×10^{-9} erg s^{-1} cm^{-2}. Errors are reported at 90% CL.
[a] The inner radius for the `diskbb` component is estimated assuming an inclination at 40°, as reported in Anderson et al. (1997), and a distance of 8 kpc (Baumgardt & Vasiliev 2021).
[b] The source luminosity for $D = 8$ kpc.

5. Spectro-polarimetric Analysis

The IXPE Stokes parameters I, Q, and U spectra have been fitted with XSPEC v.12.13.0c (Arnaud 1996) freezing the spectral model at the one reported in Section 4 and summarized in Table 2, and applying the same gain corrections to the response files of the I, Q, and U spectra. As discussed above, we tested different models, but for the spectro-polarimetric analysis in this section, we opt for the simplest model satisfactorily fitting the data, which is `tbabs*(diskbb +Gauss+comptb)`.

The I spectrum alone gives a $\chi^2/\mathrm{dof} = 226/212 = 1.07$. The first spectro-polarimetric analysis, including Q and U spectra, has been performed to confirm an increase of the polarization with energy; thus, we tested two models, the first one assuming a constant polarization using the `polconst` model from XSPEC for both the `diskbb` and `comptb` components, obtaining a PD of $0.5\% \pm 0.3\%$, PA $= -75° \pm 27°$, and $\chi^2/\mathrm{dof} = 740/664 = 1.11$. Hereafter, all the errors are reported at 90% CL. Then, we considered the possibility that polarization linearly depends on energy using the `pollin` model: $\mathrm{PD}(E) = A_1 + A_{\rm slope}(E - 1)$;

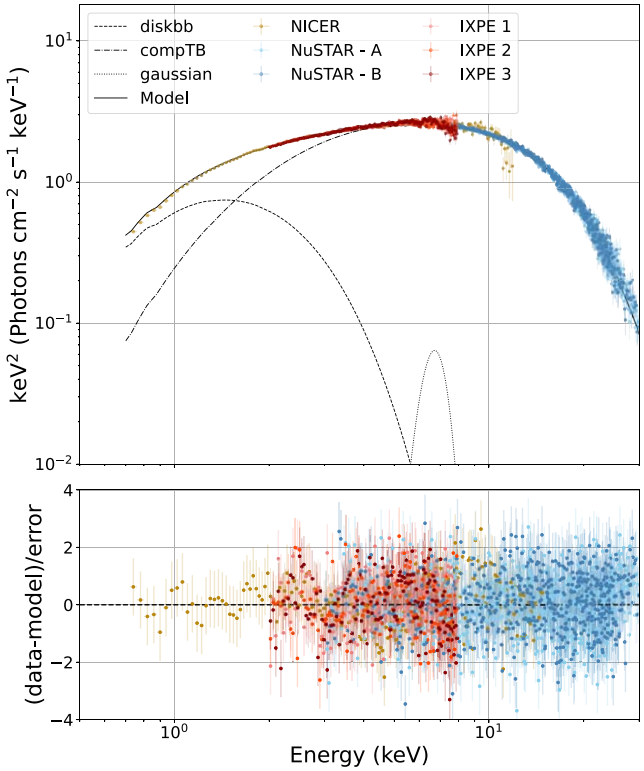

Figure 8. Spectral energy distribution of 4U 1820−303 in EF_E representation. The points show the data from NICER (brown), NuSTAR (blue), and IXPE (red). The different spectral model components are reported in black lines for `diskbb` (dashed), `comptb` (dotted–dashed), and `Gauss` (dotted). The bottom panel shows the residuals between the data and the best-fit model.

$\mathrm{PA}(E) = \psi_1 + \psi_{\mathrm{slope}}(E-1)$ (where the energy E is in keV). We obtain the PD at 1 keV of $A_1 = 2.9\% \pm 1.0\%$ with a slope of $A_{\mathrm{slope}} = -1.3\% \pm 0.3\%\ \mathrm{keV}^{-1}$, and a PA of $\psi_1 = 43° \pm 27°$ at 1 keV with a slope $\psi_{\mathrm{slope}} = -3° \pm 5°\ \mathrm{keV}^{-1}$, with a $\chi^2/\mathrm{dof} = 704/662 = 1.063$. These results are compatible with the PA being constant, while the PD has a negative slope. We note that the best-fit PD at 1 keV and the PD slope imply that the PD becomes close to zero at about 3 keV and reaches a value of ∼6% at 7–8 keV at a PA of −47° (change of sign of PD is equivalent to a 90° swing of the PA). This confirms the results obtained with `PCUBE` shown in Figures 6 and 5(c). The F-test for these two fits gives a value of 17.13 (probability 5.6×10^{-8}), confirming that the energy-dependent polarization is favored by the data.

Considering that the PD at low energy is not significant (see Figure 5(c) and Table 1), we tested the hypothesis that only the `comptb` component is constantly polarized, but in this scenario, χ^2/dof reaches a value higher than 4, confirming the need for a polarized `diskbb` component in the spectro-polarimetric fit. At this point, we tried to disentangle the polarization of the `diskbb` and `comptb` components by associating each component with its own polarization. We assumed for the disk a constant polarization, and for the Comptonization, we considered three different polarimetric models: `polconst` with a constant polarization, `pollin`, i.e., polarization depends linearly on energy, and `polpow` model that assumes that polarization is changing as a power law of energy $\mathrm{PD}(E) = A_{\mathrm{norm}} E^{-A_{\mathrm{index}}}$, and $\mathrm{PA}(E) = \psi_{\mathrm{norm}} E^{-\psi_{\mathrm{index}}}$. In order to reduce the number of parameters, we fixed ψ_{slope} and ψ_{index} at zero. The results from this analysis are reported in Table 3 and Figure 9.

All considered models give similar results, with polarization at low energies being orthogonal to that at higher energies. For the `polconst` model, the disk polarization reaches ∼10%; the Comptonization component is significantly polarized at a 5% level, with the PA being orthogonal to that of the disk. In the case of the `pollin` model for the `comptb` component, the disk polarization becomes compatible with smaller values, as expected in literature, while, at the same time, the PD of the Comptonization component changes sign around 4 keV corresponding to the rotation of the PA from 28° at lower energies to −62° at higher energies confirming the result of `PCUBE`. For the `polpow` model, we obtain a PD strongly increasing with energy (note the negative PD index $A_{\mathrm{index}} \approx -5$) from a PD at 1 keV of just $\sim 10^{-3}$%. The uncertainties on the parameters are quite large due to the correlation between PD and PA, but also because the statistical uncertainty of the data does not allow us to clearly disentangle different models.

6. Radio Observation

4U 1820−303 was observed with the ATCA on 2021 April 15 from 12:49:40 and 21:51:20 UT (under project code CX530). During this observation, ATCA was in a relatively compact H214 configuration. The data were recorded simultaneously at two central frequencies, 5.5 and 9 GHz, with 2 GHz of bandwidth at each frequency. We used the unpolarized PKS B1934−638 for primary calibration and to solve for antenna leakages. The nearby calibrator B1817−254 was used for gain calibration. Calibration and imaging followed standard procedures using the Common Astronomy Software Applications for radio astronomy (CASA, version 5.1.2; CASA Team et al. 2022). The polarization calibration used the CASA task `atcapolhelpers.py` and `qufromgain` routine.[65] The imaging used a Briggs robust parameter of 2 to maximize the image sensitivity. The isolated antenna (6) (located 6 km from the array core) was used during imaging.

While 4U 1820−303 was detected at both frequency bands, the radio counterpart was relatively faint. Fitting for a point source in the image plane (Stokes I), we measured a flux density of $100 \pm 12\ \mu$Jy at 5.5 GHz and $80 \pm 10\ \mu$Jy at 9 GHz. This corresponds to a radio spectral index of –0.45 ± 0.30. The X-ray brightness, state, and radio spectral index at the time of the observations suggest that the radio emission originates from either a quenched compact jet or transient ejecta (see, e.g., Russell et al. 2021). Imaging the field in both Stokes Q and U, no significant linear polarization was detected. We place a 3σ upper limits on the fractional linear polarization of 60% and 70% at both 5.5 and 9 GHz, respectively. Stacking the two bands gives a 3σ upper limit of 50% (at 7.25 GHz).

7. Discussion

In this paper, we report the first detection of polarization in the X-rays with IXPE and a new constraint on radio polarization by ATCA for the atoll-source 4U 1820−303. The spectral analysis performed using the data from different X-rays observatories confirms the presence of a broad Fe line, as reported in Cackett et al. (2008), Titarchuk et al. (2013), and Mondal et al. (2016), in the NuSTAR data. In the radio, the

[65] From https://github.com/radio-astro.

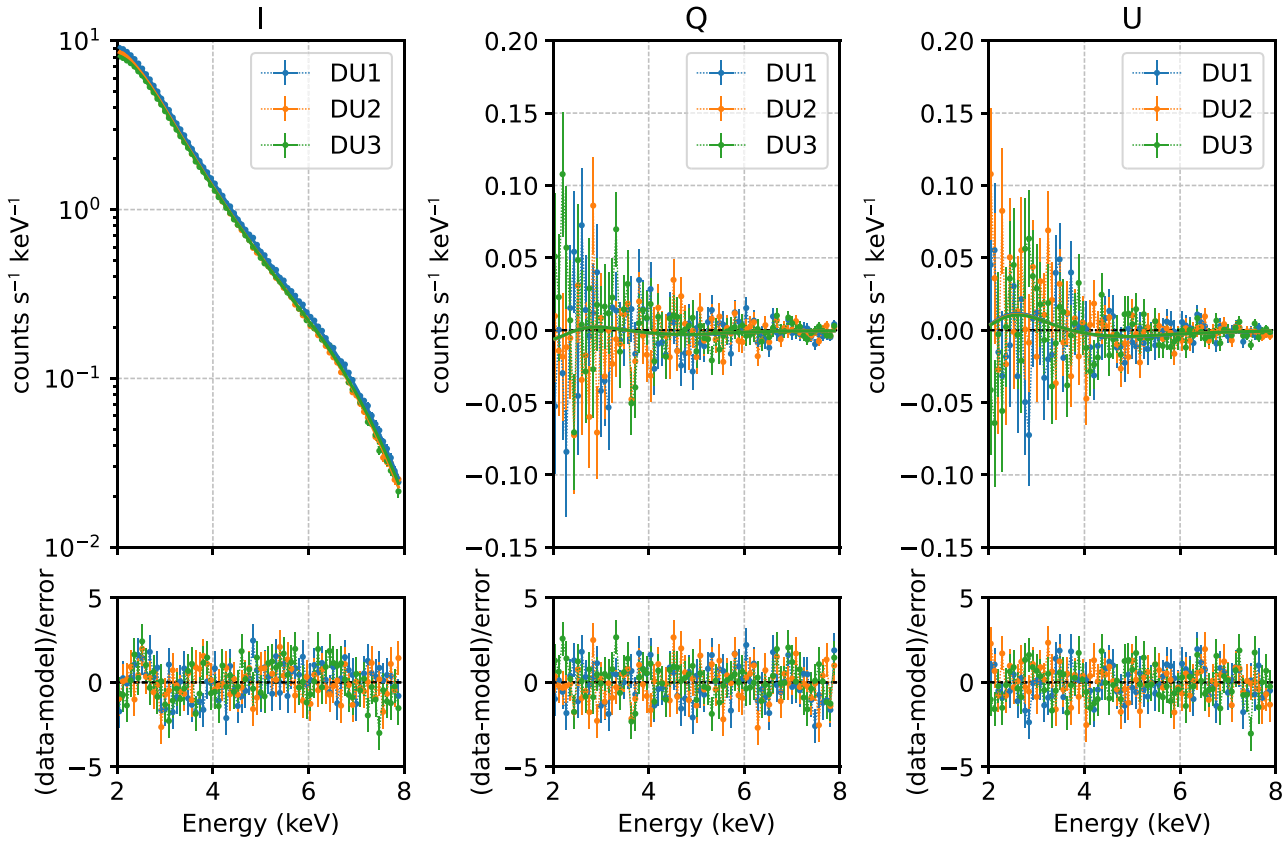

Figure 9. Spectral joint fit for the Stokes parameters I, Q, and U in the 2–8 keV energy band using three IXPE detectors and applying the model `tbabs*(Gauss+polconst*diskbb+polpow*comptb)`. The best fit gives $\chi^2/\mathrm{dof} = 1.054$ (see also Table 3).

Table 3
Main Results of the Spectro-polarimetric Analysis

Polarimetric Components		`polconst*diskbb + polconst*comptb`	`polconst*diskbb + pollin*comptb`	`polconst*diskbb + polpow*comptb`
`diskbb`	PD (%)	9.8±4.2	$8.1^{+7.1}_{-6.8}$	$3.2^{+3.0}_{-2.9}$
	PA (deg)	32 ± 13	-59^{+13}_{-26}	43 ± 35
`comptb`	PD/A_1 (%)[a]	5.31 ± 0.24	5.7 ± 2.4	$0.46^{+9.63}_{-0.46} \times 10^{-3}$
	A_{slope}(% keV^{-1})	…	-1.9 ± 0.6	…
	A_{index}	…	…	$-4.9^{+1.6}_{-2.6}$
	PA/ψ_1 (deg)[a]	-63 ± 11	38 ± 7	-63 ± 7
	ψ_{slope}(deg keV^{-1})	…	0 (f)[b]	…
	ψ_{index}	…	…	0 (f)[b]
	χ^2/dof	$724/662 = 1.094$	$699/661 = 1.057$	$697/661 = 1.054$

Notes. Errors are at 90% CL.
[a] For the `pollin` and `polpow` models, A_1 and ψ_1 refer to the PD and PA values at 1 keV.
[b] We fixed the slope and the index of the PA at zero.

source showed an emission that is consistent with either a quenched compact jet or a transient ejecta.

IXPE results on the X-ray polarization obtained using the model-independent IXPEOBSSIM–PCUBE analysis show a different behavior of this source with respect to the other atoll and Z-sources observed up to now (Capitanio et al. 2023; Chatterjee et al. 2023; Cocchi et al. 2023; Farinelli et al. 2023; Jayasurya et al. 2023; Ursini et al. 2023). In particular, this is the first source showing a strong increase of the polarization with energy up to 10% in the 7–8 keV energy band. At low energy, there is no secure detection of polarization, even if there is a hint of a ∼0.8% PD at 96% CL, with a PA orthogonal to the ones at higher energies.

We also attempted a spectro-polarimetric analysis of the source emission. Assuming simple polarimetric phenomenological models for the Comptonization component, a need for nonzero polarization of the disk emission (which dominates in the lower part of the IXPE band) emerged to account for the overall low PD. In this scenario, leaving the parameters unconstrained, the polarization of the disk tends to be

orthogonal to the one associated with the Comptonization. The PD varies, depending on the polarimetric models, from a few percent up to ∼10%. In the lower boundary, these values are compatible with the polarization expected in case of an electron-scattering dominated optically thick accretion disk, which is below 2% (Chandrasekhar 1960; Sobolev 1963) considering 4U 1820−303 inclination—ranging from ∼20° to 55° (Anderson et al. 1997; Cackett et al. 2008; Mondal et al. 2016). We also note that, in case of a disk whose opacity is dominated by electron scattering, the PA is expected to be orthogonal to the disk axis. Therefore, the PA of the disk component measured by IXPE, which is ∼30° east of north, would indicate that the position angle of the disk rotation axis is ≃−60° (or 120°).

The Comptonized component is firmly associated with a high and energy-dependent polarization. For an optically thin corona, the PD can reach 10%–20% in slab geometry (Poutanen & Svensson 1996; Schnittman & Krolik 2010; Gnarini et al. 2022; Poutanen et al. 2023). However, the Thomson optical depth τ_T, required to produce the observed spectrum with the photon index of $\Gamma \approx 1.9$ and electron temperature T_e of ∼3 keV, exceeds 10. For such a high optical depth, the PD is even smaller than that given by the classical results of Chandrasekhar (1960), Sobolev (1963) for $\tau_T \gg 1$ (see Figure 5 in Sunyaev & Titarchuk 1985). Thus, the ∼10% polarization observed by IXPE at highest energies is difficult to explain for any reasonable inclination. Therefore, our results require some nonstandard coronal geometry.

One of the possibilities is the presence of a mildly relativistic outflow from the inner part of the accretion flow where Comptonization takes place. Because of relativistic aberration, the PD at a given inclination becomes larger than that in the static corona with the PA parallel to the disk normal (Beloborodov 1998; Poutanen et al. 2023). For an optically thin outflow, the PD of the scattered component can reach 15%, but the PD of the total emission will be reduced by unscattered radiation. Thus, we are forced to assume that the outflow is optically thick; in this case, the total PD can reach 10%–15% even at moderate inclinations of 40°–60° (with the PA being still parallel to the disk normal, see Figure 4 in Beloborodov 1998). The remaining question is why the PD is high only in the 7–8 keV band, but not below.

An alternative to the outflow would be the presence of a strong reflection already claimed to be present in previous weakly magnetized NSs observed by IXPE (Gnarini et al. 2022; Cocchi et al. 2023; Farinelli et al. 2023; Ursini et al. 2023). As already discussed in Section 4, such a component was investigated, and its relative flux in the IXPE band is estimated to be below 5% even above 4 keV. Because a typical PD for the reflected component is about 20% (Matt 1993; Poutanen et al. 1996), it cannot alone easily explain the observed PD of 10% above 7 keV and its fast rise with energy. Notwithstanding, adding a polarized contribution from the reflection component aligned with that of the corona could partially reduce the PD of the Comptonized component to a level more easily explained with standard geometries.

Overall, the spectro-polarimetric modeling supports a geometry having an SL perpendicular to the disk plane, already described in the context of previous IXPE observations of atoll sources, with the important difference of the PD for the Comptonized component which is about 10% for 4U 1820−303 instead of a nondetection for GS 1826−238 (Capitanio et al. 2023), ≃3% for GX 9+9 and Cyg X-2 in the energy band 4–8 keV (Farinelli et al. 2023; Ursini et al. 2023), and ≃5% for XTE J1701−462 in the 4–8 keV band in the horizontal branch. This can be contrasted to a ≃50% of Comptonized fraction in GS 1826−238 (Capitanio et al. 2023) and <70% in GX 9+9, where the reflection component is well determined (Ursini et al. 2023). This might imply a correlation between the corona dominated spectrum and the high PD, but further observations are needed to disentangle the polarization associated with each spectral component.

Linearly polarized radio emission was not detected, with an upper limit at 99.73% CL of 50% on the PD in the radio band; unfortunately, this result does not allow us to do a direct comparison between the PA in the radio and the X-rays. As such, due to the radio faintness, we cannot compare our result to the one obtained for Cyg X-2 (Farinelli et al. 2023) and Sco X-1 (Long et al. 1979, 2022), where the X-ray PA was aligned with the direction of the radio jets.

8. Summary

The IXPE result for 4U 1820−303 shows a different polarization behavior with respect to other atoll sources, GX 9+9 (Chatterjee et al. 2023; Ursini et al. 2023) and GS 1826−238 (Capitanio et al. 2023), but also with respect to the Z-sources Cyg X-2 (Farinelli et al. 2023) and XTE J1701−462 (Cocchi et al. 2023; Jayasurya et al. 2023). In particular, the need to have a polarized disk emission is more evident. Moreover, the model-independent analysis gives an indication of a 90° rotation of the PA at lowest energies, where the disk contributes the most. A very high PD of about 10% detected above 7 keV did not find an obvious explanation within standard models of X-ray emission of weakly magnetized NSs. One possibility is that the polarization is produced in an optically thick outflow emanating from the inner part of the accretion disk. Future studies of this source with a longer exposure could help to disentangle the polarization of each spectral component. Monitoring the source along its super-orbital period or when it moves along the banana and island states could help to better understand the polarization variations and, thanks to this, verify possible geometry variations as a function of the mass accretion rate.

Acknowledgments

The Imaging X-ray Polarimetry Explorer (IXPE) is a joint US and Italian mission. The US contribution is supported by the National Aeronautics and Space Administration (NASA) and led and managed by its Marshall Space Flight Center (MSFC), with industry partner Ball Aerospace (contract NNM15AA18C). The Italian contribution is supported by the Italian Space Agency (Agenzia Spaziale Italiana, ASI) through contract ASI-OHBI-2017-12-I.0, agreements ASI-INAF-2017-12-H0 and ASI-INFN-2017.13-H0, and its Space Science Data Center (SSDC) with agreements ASI-INAF-2022-14-HH.0 and ASI-INFN 2021-43-HH.0, and by the Istituto Nazionale di Astrofisica (INAF) and the Istituto Nazionale di Fisica Nucleare (INFN) in Italy. This research used data products provided by the IXPE Team (MSFC, SSDC, INAF, and INFN) and distributed with additional software tools by the High-Energy Astrophysics Science Archive Research Center (HEASARC), at NASA Goddard Space Flight Center (GSFC).

This research has made use of the MAXI data provided by RIKEN, JAXA, and the MAXI team and of the Swift/BAT transient monitor results provided by the Swift/BAT team. We thank Jamie Stevens and ATCA staff for the scheduling of these observations. ATCA is part of the Australia Telescope National Facility (https://ror.org/05qajvd42), which is funded by the Australian Government for operation as a National Facility managed by CSIRO. We acknowledge the Gomeroi people as the traditional owners of the ATCA observatory site.

The authors acknowledge the prompt schedules of the simultaneous observations: Keith G. Gendrau, Zaven Arzoumanian, and the NICER Science Operation Centre (SOC) team; Boris Sbarufatti, Kim Page, Brad Cenko, and Swift-XRT SOC team; Karl Forster, Murray Brightman, Fiona A. Harrison, and NuSTAR SOC team. We also acknowledge support from the Academy of Finland grants 333112, 349144, 349373, and 349906 (J.P., S.S.T.) and the German Academic Exchange Service (DAAD) travel grant 57525212 (V.D.).

Facilities: IXPE, Swift-XRT, NICER, NuSTAR.

Software: IXPEOBSSIM (Baldini et al. 2022), XSPEC (Arnaud 1996), HEASOFT (Blackburn 1995).

Appendix
Data Handling for X-Ray Observatories

In this study, as we reported in the previous sections, IXPE observations were coordinated with NuSTAR, NICER, and Swift-XRT aiming to verify the state of the source and also to obtain a better constraint on the spectral model thanks to better energy resolution and broadband coverage. In this section, we briefly report the data handling and extraction applied to the data we used.

A.1. IXPE

The IXPE, a NASA mission in partnership with the Italian Space Agency, was launched on 2021 December 9. A detailed description of the observatory and its performance is given in Weisskopf et al. (2022). IXPE consists of three identical grazing incidence telescopes, providing imaging and spectral polarimetry over the 2–8 keV energy band with a time resolution better than 10 μs. Each telescope comprises an X-ray module of mirror assembly and a polarization-sensitive DU equipped with a gas-pixel detector (Costa et al. 2001; Soffitta et al. 2021).

IXPE observed 4U 1820−303 twice, in 2022 October for a short period and for a longer one in 2023 April (ObsID 02002399) with a total effective exposure of 16 and 86 ks per DU, respectively. The level 2 data were processed with the IXPE dedicated software IXPEOBSSIM (Baldini et al. 2022) v. 30.3.0 and with FTOOL released in HEASOFT v. 6.31.1 using the Calibration database released on 2022 November 17.

Source photons were selected from the IXPE telescopes images collected within a circular region having radius 100″ centered on the source position, while the background, following the prescription by Di Marco et al. (2023) for the sources with high counts rate ($\gtrsim$2 count s^{-1}), has not been subtracted from the data, because it is negligible (in these observations, the background is roughly 2 orders of magnitude below the source in all energy bins).

For the spectral analysis, the flux (Stokes parameter *I*) energy spectra from the three DUs have been extracted following the weighted approach described in Di Marco et al. (2022a), and the data were binned to have at least 30 counts per energy channel, while in the spectro-polarimetric analysis, we applied a constant energy binning of 200 eV for all the three energy distributions of Stokes parameters *I*, *Q*, and *U*.

A.2. NICER

The NICER is a soft X-ray instrument on board the International Space Station, launched in 2017 June, and it consists of 56 coaligned concentrator X-ray optics, each of which is paired with a single silicon drift detector. NICER does not offer imaging capabilities, but offers a large collecting area providing unmatched time resolution in the soft X-ray bandpass, with a sensitive energy interval 0.2–12 keV.

Contemporaneous observations of 4U 1820−303 during both IXPE observations were performed in the frame of the NICER GO cycle 5 (proposal 6189 having PI Alessandro Di Marco). During the first observation, NICER observed the source for a total exposure of $\simeq$1.7 ks (ObsID 5050300117), while, during the second observation, two data sets were released (ObsIDs 6689020101 and 6689020102) covering April 15 and 16 in several snapshots for a total exposure time of $\simeq$10.3 and $\simeq$13.7 ks respectively.

The NICER data were processed with the NICER Data Analysis Software v010a released on 2022 December 16 provided under HEASOFT v6.31.1 with the CALDB version released on 2022 October 30. The background spectra have been estimated by applying the new SCORPEON model in the 0.22–15 keV band. All the obtained spectra were grouped to have at least 30 counts per bin.

A.3. Swift-XRT

The Neil Gehrels Swift Observatory (Gehrels et al. 2004) carries three instruments to enable the most detailed observations of gamma-ray bursts to date; XRT is one of them, based on a sensitive, flexible, autonomous X-ray CCD imaging spectrometer. Swift-XRT coordinated observations with IXPE for 4U 1820−303 were performed; they are used in this work to monitor the source status and to obtain spectral information during both the IXPE observations. Given the source brightness, the Swift-XRT observations were performed in windowed timing mode. Four Swift-XRT pointings covered the first IXPE observation in the period 2022 October 11–13 (ObsIDs: 00014980028, 00014980029, 00014980030, and 00014980031), while the second IXPE observation consisted of 5 pointings on 2023 April 15 and 16 grouped in 3 data sets (ObsIDs: 00014980055, 00014980056, and 00014980057). These data have been used to monitor the source HR along the two IXPE observations, as reported in Figure 4. The data were extracted using `xselect` v2.5b released with HEASOFT v6.31.1. The source and background extractions were performed using the imaging capabilities of Swift-XRT. Given the source counting rate $\geqslant$100 count s^{-1}, data can be affected by pile-up as reported in the appendix of Romano et al. (2006).

A.4. NuSTAR

NuSTAR observatory (Harrison et al. 2013) consists of two identical XRT modules, referred to as FPMA and FPMB, providing broadband X-ray imaging, spectroscopy, and timing in the energy range of 3–79 keV with an angular resolution of 18″ (FWHM) and spectral resolution of 400 eV (FWHM) at 10 keV. During both the IXPE observations of 4U 1820−303,

NuSTAR performed coordinated observations, one (ObsID: 90802327002) from 2022 October 12 at 14:31 UTC to October 13 at 2:41 UTC with a total exposure of ≃16.9 ks and the other two on 2023 April 15 and 16 (ObsIDs: 90902308002 and 90902308004) with a total exposure of ≃16.8 and ≃15.2 ks, respectively.

The NuSTAR data were processed with the standard Data Analysis Software (`nustardas` 16Feb22 v2.1.2) provided under HEASOFT v6.31.1 with the CALDB version released on 2023 April 4. A circular 150″ radius region has been used for both source and background spectra extractions, with the source region centered on the locations of 4U 1820−303, and the background one in an off-center sourceless region in the detector image. All the obtained spectra were grouped to have at least 30 counts per bin.

ORCID iDs

Alessandro Di Marco https://orcid.org/0000-0003-0331-3259
Fabio La Monaca https://orcid.org/0000-0001-8916-4156
Juri Poutanen https://orcid.org/0000-0002-0983-0049
Thomas D. Russell https://orcid.org/0000-0002-7930-2276
Alessio Anitra https://orcid.org/0000-0002-2701-2998
Ruben Farinelli https://orcid.org/0000-0003-2212-367X
Guglielmo Mastroserio https://orcid.org/0000-0003-4216-7936
Fabio Muleri https://orcid.org/0000-0003-3331-3794
Fei Xie https://orcid.org/0000-0002-0105-5826
Matteo Bachetti https://orcid.org/0000-0002-4576-9337
Luciano Burderi https://orcid.org/0000-0001-5458-891X
Francesco Carotenuto https://orcid.org/0000-0002-0426-3276
Melania Del Santo https://orcid.org/0000-0002-1793-1050
Tiziana Di Salvo https://orcid.org/0000-0002-3220-6375
Michal Dovčiak https://orcid.org/0000-0003-0079-1239
Andrea Gnarini https://orcid.org/0000-0002-0642-1135
Rosario Iaria https://orcid.org/0000-0003-2882-0927
Jari J. E. Kajava https://orcid.org/0000-0002-3010-8333
Kuan Liu https://orcid.org/0009-0007-8686-9012
Riccardo Middei https://orcid.org/0000-0001-9815-9092
Stephen L. O'Dell https://orcid.org/0000-0002-1868-8056
Maura Pilia https://orcid.org/0000-0001-7397-8091
John Rankin https://orcid.org/0000-0002-9774-0560
Andrea Sanna https://orcid.org/0000-0002-0118-2649
Jakob van den Eijnden https://orcid.org/0000-0002-5686-0611
Martin C. Weisskopf https://orcid.org/0000-0002-5270-4240
Fiamma Capitanio https://orcid.org/0000-0002-6384-3027
Enrico Costa https://orcid.org/0000-0003-4925-8523
Philip Kaaret https://orcid.org/0000-0002-3638-0637
Alessio Marino https://orcid.org/0000-0001-5674-4664
Paolo Soffitta https://orcid.org/0000-0002-7781-4104
Francesco Ursini https://orcid.org/0000-0001-9442-7897
Filippo Ambrosino https://orcid.org/0000-0001-7915-996X
Massimo Cocchi https://orcid.org/0000-0002-5817-3129
Sergio Fabiani https://orcid.org/0000-0003-1533-0283
Herman L. Marshall https://orcid.org/0000-0002-6492-1293
Giorgio Matt https://orcid.org/0000-0002-2152-0916
Sara Elisa Motta https://orcid.org/0000-0002-6154-5843
Alessandro Papitto https://orcid.org/0000-0001-6289-7413
Luigi Stella https://orcid.org/0000-0002-0018-1687
Silvia Zane https://orcid.org/0000-0001-5326-880X
Iván Agudo https://orcid.org/0000-0002-3777-6182
Lucio A. Antonelli https://orcid.org/0000-0002-5037-9034
Luca Baldini https://orcid.org/0000-0002-9785-7726
Wayne H. Baumgartner https://orcid.org/0000-0002-5106-0463
Ronaldo Bellazzini https://orcid.org/0000-0002-2469-7063
Stefano Bianchi https://orcid.org/0000-0002-4622-4240
Stephen D. Bongiorno https://orcid.org/0000-0002-0901-2097
Raffaella Bonino https://orcid.org/0000-0002-4264-1215
Alessandro Brez https://orcid.org/0000-0002-9460-1821
Niccolò Bucciantini https://orcid.org/0000-0002-8848-1392
Simone Castellano https://orcid.org/0000-0003-1111-4292
Elisabetta Cavazzuti https://orcid.org/0000-0001-7150-9638
Chien-Ting Chen https://orcid.org/0000-0002-4945-5079
Stefano Ciprini https://orcid.org/0000-0002-0712-2479
Alessandra De Rosa https://orcid.org/0000-0001-5668-6863
Ettore Del Monte https://orcid.org/0000-0002-3013-6334
Laura Di Gesu https://orcid.org/0000-0002-5614-5028
Niccolò Di Lalla https://orcid.org/0000-0002-7574-1298
Immacolata Donnarumma https://orcid.org/0000-0002-4700-4549
Victor Doroshenko https://orcid.org/0000-0001-8162-1105
Steven R. Ehlert https://orcid.org/0000-0003-4420-2838
Teruaki Enoto https://orcid.org/0000-0003-1244-3100
Yuri Evangelista https://orcid.org/0000-0001-6096-6710
Riccardo Ferrazzoli https://orcid.org/0000-0003-1074-8605
Javier A. Garcia https://orcid.org/0000-0003-3828-2448
Shuichi Gunji https://orcid.org/0000-0002-5881-2445
Jeremy Heyl https://orcid.org/0000-0001-9739-367X
Wataru Iwakiri https://orcid.org/0000-0002-0207-9010
Svetlana G. Jorstad https://orcid.org/0000-0001-6158-1708
Vladimir Karas https://orcid.org/0000-0002-5760-0459
Fabian Kislat https://orcid.org/0000-0001-7477-0380
Jeffery J. Kolodziejczak https://orcid.org/0000-0002-0110-6136
Henric Krawczynski https://orcid.org/0000-0002-1084-6507
Luca Latronico https://orcid.org/0000-0002-0984-1856
Ioannis Liodakis https://orcid.org/0000-0001-9200-4006
Simone Maldera https://orcid.org/0000-0002-0698-4421
Alberto Manfreda https://orcid.org/0000-0002-0998-4953
Frédéric Marin https://orcid.org/0000-0003-4952-0835
Andrea Marinucci https://orcid.org/0000-0002-2055-4946
Alan P. Marscher https://orcid.org/0000-0001-7396-3332
Francesco Massaro https://orcid.org/0000-0002-1704-9850
Tsunefumi Mizuno https://orcid.org/0000-0001-7263-0296
Michela Negro https://orcid.org/0000-0002-6548-5622
Chi-Yung Ng https://orcid.org/0000-0002-5847-2612
Nicola Omodei https://orcid.org/0000-0002-5448-7577
Chiara Oppedisano https://orcid.org/0000-0001-6194-4601
George G. Pavlov https://orcid.org/0000-0002-7481-5259
Abel L. Peirson https://orcid.org/0000-0001-6292-1911
Matteo Perri https://orcid.org/0000-0003-3613-4409
Melissa Pesce-Rollins https://orcid.org/0000-0003-1790-8018
Pierre-Olivier Petrucci https://orcid.org/0000-0001-6061-3480
Andrea Possenti https://orcid.org/0000-0001-5902-3731

Simonetta Puccetti https://orcid.org/0000-0002-2734-7835
Brian D. Ramsey https://orcid.org/0000-0003-1548-1524
Ajay Ratheesh https://orcid.org/0000-0003-0411-4243
Oliver J. Roberts https://orcid.org/0000-0002-7150-9061
Roger W. Romani https://orcid.org/0000-0001-6711-3286
Carmelo Sgrò https://orcid.org/0000-0001-5676-6214
Patrick Slane https://orcid.org/0000-0002-6986-6756
Gloria Spandre https://orcid.org/0000-0003-0802-3453
Douglas A. Swartz https://orcid.org/0000-0002-2954-4461
Toru Tamagawa https://orcid.org/0000-0002-8801-6263
Fabrizio Tavecchio https://orcid.org/0000-0003-0256-0995
Roberto Taverna https://orcid.org/0000-0002-1768-618X
Allyn F. Tennant https://orcid.org/0000-0002-9443-6774
Nicholas E. Thomas https://orcid.org/0000-0003-0411-4606
Francesco Tombesi https://orcid.org/0000-0002-6562-8654
Alessio Trois https://orcid.org/0000-0002-3180-6002
Sergey S. Tsygankov https://orcid.org/0000-0002-9679-0793
Roberto Turolla https://orcid.org/0000-0003-3977-8760
Jacco Vink https://orcid.org/0000-0002-4708-4219
Kinwah Wu https://orcid.org/0000-0002-7568-8765

References

Anderson, S. F., Margon, B., Deutsch, E. W., Downes, R. A., & Allen, R. G. 1997, ApJL, 482, L69
Arnaud, K. A. 1996, in ASP Conf. Ser. 101, Astronomical Data Analysis Software and Systems V, ed. G. H. Jacoby & J. Barnes (San Francisco, CA: ASP), 17
Bahramian, A., & Degenaar, N. 2022, in Low-Mass X-ray Binaries, ed. C. Bambi & A. Santangelo (Singapore: Springer), 1
Baldini, L., Bucciantini, N., Lalla, N. D., et al. 2022, SoftX, 19, 101194
Baumgardt, H., & Vasiliev, E. 2021, MNRAS, 505, 5957
Beloborodov, A. M. 1998, ApJL, 496, L105
Blackburn, J. K. 1995, in ASP Conf. Ser. 77, Astronomical Data Analysis Software and Systems IV, ed. R. A. Shaw, H. E. Payne, & J. J. E. Hayes (San Francisco, CA: ASP), 367
Burns, E., Svinkin, D., Fenimore, E., et al. 2023, ApJL, 946, L31
Cackett, E. M., Miller, J. M., Bhattacharyya, S., et al. 2008, ApJ, 674, 415
Capitanio, F., Fabiani, S., Gnarini, A., et al. 2023, ApJ, 943, 129
CASA Team, Bean, B., Bhatnagar, S., et al. 2022, PASP, 134, 114501
Chandrasekhar, S. 1960, Radiative Transfer (New York: Dover)
Chatterjee, R., Agrawal, V. K., Jayasurya, K. M., & Katoch, T. 2023, MNRAS, 521, L74
Chou, Y., & Grindlay, J. E. 2001, ApJ, 563, 934
Cocchi, M., Gnarini, A., Fabiani, S., et al. 2023, A&A, 674, L10
Costa, E., Soffitta, P., Bellazzini, R., et al. 2001, Natur, 411, 662
Curran, P. A., Coriat, M., Miller-Jones, J. C. A., et al. 2014, MNRAS, 437, 3265
D'Aì, A., diSalvo, T., Ballantyne, D., et al. 2010, A&A, 516, A36
Di Marco, A., Costa, E., Muleri, F., et al. 2022a, AJ, 163, 170
Di Marco, A., Muleri, F., Fabiani, S., et al. 2022b, Proc. SPIE, 12181, 121811C
Di Marco, A., Soffitta, P., Costa, E., et al. 2023, AJ, 165, 143
Díaz Trigo, M., Migliari, S., Miller-Jones, J. C. A., et al. 2017, A&A, 600, A8
Egron, E., Di Salvo, T., Motta, S., et al. 2013, A&A, 550, A5
Farinelli, R., Fabiani, S., Poutanen, J., et al. 2023, MNRAS, 519, 3681
Gehrels, N., Chincarini, G., Giommi, P., et al. 2004, ApJ, 611, 1005
Gnarini, A., Ursini, F., Matt, G., et al. 2022, MNRAS, 514, 2561
Grindlay, J., Gursky, H., Schnopper, H., et al. 1976, ApJL, 205, L127
Haardt, F., & Matt, G. 1993, MNRAS, 261, 346
Harrison, F. A., Craig, W. W., Christensen, F. E., et al. 2013, ApJ, 770, 103
Hasinger, G., & van der Klis, M. 1989, A&A, 225, 79
Hughes, J. P., Long, K. S., & Novick, R. 1984, ApJ, 280, 255
Iaria, R., Di Salvo, T., Del Santo, M., et al. 2016, A&A, 596, A21
Inogamov, N. A., & Sunyaev, R. A. 1999, AstL, 25, 269
Jayasurya, K. M., Agrawal, V. K., & Chatterjee, R. 2023, arXiv:2302.03396
Krimm, H. A., Holland, S. T., Corbet, R. H. D., et al. 2013, ApJS, 209, 14
Lapidus, I. I., & Sunyaev, R. A. 1985, MNRAS, 217, 291
Long, K. S., Chanan, G. A., Ku, W. H. M., & Novick, R. 1979, ApJL, 232, L107
Long, X., Feng, H., Li, H., et al. 2022, ApJL, 924, L13
Longair, M. S. 2011, High Energy Astrophysics (Cambridge: Cambridge Univ. Press)
Loskutov, V. M., & Sobolev, V. V. 1982, Afz, 18, 81
Madsen, K. K., Forster, K., Grefenstette, B., Harrison, F. A., & Miyasaka, H. 2022, JATIS, 8, 034003
Matsuoka, M., Kawasaki, K., Ueno, S., et al. 2009, PASJ, 61, 999
Matt, G. 1993, MNRAS, 260, 663
Migliari, S., Fender, R. P., Rupen, M., et al. 2004, MNRAS, 351, 186
Mondal, A. S., Dewangan, G. C., Pahari, M., et al. 2016, MNRAS, 461, 1917
Popham, R., & Sunyaev, R. 2001, ApJ, 547, 355
Poutanen, J., Nagendra, K. N., & Svensson, R. 1996, MNRAS, 283, 892
Poutanen, J., & Svensson, R. 1996, ApJ, 470, 249
Poutanen, J., Veledina, A., & Beloborodov, A. M. 2023, ApJL, 949, L10
Poutanen, J., & Vilhu, O. 1993, A&A, 275, 337
Rappaport, S., Nelson, L. A., Ma, C. P., & Joss, P. C. 1987, ApJ, 322, 842
Romano, P., Campana, S., Chincarini, G., et al. 2006, A&A, 456, 917
Russell, T. D., Degenaar, N., van den Eijnden, J., et al. 2021, MNRAS, 508, L6
Schnittman, J. D., & Krolik, J. H. 2010, ApJ, 712, 908
Shakura, N. I., & Sunyaev, R. A. 1988, AdSpR, 8, 135
Shaposhnikov, N., & Titarchuk, L. 2004, ApJL, 606, L57
Smale, A. P., Zhang, W., & White, N. E. 1997, ApJL, 483, L119
Sobolev, V. V. 1963, A Treatise on Radiative Transfer (Princeton, NJ: Van Nostrand)
Soffitta, P., Baldini, L., Bellazzini, R., et al. 2021, AJ, 162, 208
Stella, L., Priedhorsky, W., & White, N. E. 1987, ApJL, 312, L17
Suleimanov, V., & Poutanen, J. 2006, MNRAS, 369, 2036
Sunyaev, R. A., & Titarchuk, L. G. 1985, A&A, 143, 374
Tarana, A., Bazzano, A., Ubertini, P., & Zdziarski, A. A. 2007, ApJ, 654, 494
Titarchuk, L., Seifina, E., & Frontera, F. 2013, ApJ, 767, 160
Ursini, F., Farinelli, R., Gnarini, A., et al. 2023, A&A, 676, A20
van der Klis, M. 1989, ARA&A, 27, 517
Weisskopf, M. C., Soffitta, P., Baldini, L., et al. 2022, JATIS, 8, 026002
Wilms, J., Allen, A., & McCray, R. 2000, ApJ, 542, 914
Zdziarski, A. A., Gierliński, M., Wen, L., & Kostrzewa, Z. 2007, MNRAS, 377, 1017